








Analysis of thermodiffusive instabilities and flame front wrinkling in a hydrogen-fueled engine

Pedro Ye *, Jannick Erhard, Cooper Welch , Hao Shi , Andreas Dreizler , Benjamin Böhm 

Technical University of Darmstadt, Department of Mechanical Engineering, Reactive Flows and Diagnostics, Otto-Berndt-Str. 3, 64287 Darmstadt, Germany

ARTICLE INFO

Keywords:

Hydrogen
Internal combustion engine
Laser-induced fluorescence
Thermodiffusive instabilities
Flame wrinkling

ABSTRACT

This study investigates the interplay between thermodiffusive instabilities (TDI) and flame front wrinkling in a hydrogen-fueled internal combustion engine (ICE). High-speed planar laser-induced fluorescence (LIF) of the SO_2 tracer was employed to visualize flames in an optically accessible, spark-ignited ICE operating under a lean H_2 mixture at 400 rpm and 800 rpm. The results reveal that TDI cells are distinctly more pronounced at 400 rpm and in slower flames, while at 800 rpm, increased turbulence suppresses cell development and enhances overall flame wrinkling. A negative correlation between these two features indicates that TDI cells flourish in less disturbed conditions, whereas turbulence-driven wrinkling disrupts their formation. These findings suggest that at higher, more realistic engine speeds, TDI cell formation is significantly mitigated. However, other instability-driven effects, such as localized heat release variations, wall heat transfer, and flame quenching, may still play a crucial role in H_2 engine combustion. Understanding these interactions is essential for accurately modeling and optimizing hydrogen-fueled ICEs.

1. Introduction

The decarbonization of the transport sector plays a major role in the reduction of CO_2 emissions. H_2 has been regarded as a promising fuel to power the internal combustion engine (ICE), due to its carbon-free composition and relatively low-cost implementation [1,2]. Considering the higher adiabatic flame temperatures, H_2 -fueled ICEs need to run in diluted or lean mixtures to minimize the formation of thermal NO_x . In the latter case, TDI develop because of the higher molecular diffusivity of H_2 relative to the mixture's thermal diffusivity [3].

Regarding laminar H_2 flames, experiments defined spherical flame sizes from which TDI act in the formation of a cellular flame front structure [4]. These cells augment the surface density of the flame leading to an increase in flame speed. Different conditions, set in direct numerical simulations (DNS), such as unburned gas temperature and pressure have been shown to determine the properties of such cells [5].

Nevertheless, the interaction between cellular structures and turbulence remains a challenge in practical combustion applications such as ICEs. DNS under engine-like conditions indicate that turbulence can promote the onset of TDI cell formation [6], while experiments on turbulent jet flames show that higher turbulence levels disrupt these instabilities [7]. Furthermore, it has been demonstrated that a heightened sensitivity of turbulent flame speed to fluctuations in turbulent velocity is linked to lower Lewis numbers [8]. In engine applications, Schlieren imaging has revealed convection and stretching

of H_2 flames [9]. Chemiluminescence measurements by [10] revealed a strong correlation between early flame development and overall engine cycle performance. Laser-induced fluorescence (LIF) was employed by [11], suggesting that turbulence and volume confinement may counteract TDI effects. Despite these efforts, reliable detection of cell formation in engines remains elusive, and its interplay with flame front wrinkling is not fully understood. Although hydrodynamic instabilities at typical engine turbulence levels can enhance flame wrinkling [12,13], it is unclear how these effects interact with cellular development. One might intuitively expect that an increased flame surface area from cellular structures would boost wrinkling and thereby flame propagation; however, the dynamic engine flow may instead disrupt cell formation. Addressing this challenge requires high optical and temporal resolution to capture the development of TDI cells.

Due to the lean nature of the mixture and dynamic engine environment, H_2 flame detection with LIF of hydroxyl radicals (OH) is not suitable. The signal drops sharply and the image quality is reduced drastically [14]. Alternatively, SO_2 is an inert tracer suitable for LIF. Its properties allows for flame detection at high repetition rates [15]. Another challenge regards image processing. In order to enhance the signal-to-noise ratio, denoising of the images is done. However, common denoising techniques are not edge preserving, effectively lowering the optical resolution. Wavelet-based denoising techniques take into

* Corresponding author.

E-mail address: ye@rsm.tu-darmstadt.de (P. Ye).

Table 1

Operating conditions. °CA is positive for crank angle degrees after compression top dead center (TDC).

OC	N	p_{in}	λ	t_{ign}	Le_{eff}
[-]	[rpm]	[bar]	[-]	[°CA]	[-]
α	400	0.95	2.5	-25.6	0.39
A	800	0.95	2.5	-16.6	0.40

account the characteristics of the image acquiring setup [16] and have the potential to greatly enhance the detection of small structures such as TDI cells.

This paper investigates the effects of engine speed in the formation of TDI cells and flame front wrinkling. As such, H_2 flame images in an optical ICE are detected with sufficiently high spatial resolution with SO_2 -LIF. Equally, temporal resolution is high enough to obtain images at a sub-crank angle resolution. After detailing the experimental setup and methodology, the results are discussed. Flame images are firstly shown followed by a statistical analysis of the differences across and within engine speeds. This applies for TDI cell development and flame wrinkling analysis. Then, correlation analysis between both conditions is done, showcasing example cases of the obtained results. This work finishes with concluding remarks and its implications for H_2 -ICE development.

2. Experimental setup and methodology

2.1. Experimental setup

Measurements were performed in a four-stroke, single-cylinder, spark-ignited optically accessible engine with a compression ratio of 8.7 and a spray-guided, 4-valve pent-roof cylinder head. Optical access was provided by a quartz glass liner and a flat piston window (see [17,18] for details). The engine operated at 400 rpm and 800 rpm with an intake pressure of 0.95 bar. H_2 was injected 540 mm upstream of the intake valves to obtain a homogeneous air-fuel mixture at $\lambda = 2.5$. Operating conditions (OC) are summarized in Table 1, with spark timing adjusted to yield the same maximum in-cylinder pressure, p_{Cyl} (20.5 bar). The effective Lewis number, Le_{eff} , was computed at ignition timing t_{ign} following [19]. Gas properties were obtained via Cantera [20] using the measured cylinder pressure and an estimated cylinder temperature (assuming isentropic behavior with $\gamma = 1.4$) [21].

Fig. 1 illustrates the experimental and optical arrangement. SO_2 was injected upstream of the intake valve to ensure a homogeneous mixture, at volumetric concentrations of 1.1 vol% for OC α and 0.6 vol% for OC A. Under ultraviolet (UV) excitation, SO_2 fluoresces with a stronger signal at higher temperatures, enabling flame visualization via SO_2 -LIF [11,15]. Excitation at 266 nm was provided by a fourth-harmonic Nd:YAG laser (Edgewave, INNOSLAB) pulsed at 6 kHz and 8 kHz (every 0.4 °CA and 0.6 °CA) for OC α and A, respectively, with 580 μ J per pulse. The beam was shaped into a laser sheet (width: 5 mm, thickness: 160 μ m FWHM) and directed vertically through the piston mirror in the tumble plane at the exhaust side of the spark plug.

A high-speed UV camera (Phantom T3610-UV, Vision Research) equipped with a 100 mm UV lens (CERCO 2178, $f = 2.8$) and distance rings (96 mm) achieved a magnification of 1.17. A 276 nm long-pass filter isolated the fluorescence signal, while a +2000 mm correction lens reduced cylinder glass-induced astigmatism. The resulting region of interest (ROI) covered approximately 5 mm \times 15 mm with a scaling of 64.1 px/mm. Optical resolution, determined using a Siemens star at a 10% MTF threshold, had a PSF FWHM of 75.7 μ m (10.6 lp/mm), which is sufficient to resolve laminar TDI cell structures similar in size to those observed in DNS studies at 20 bar and 700 K [5].

For each operating condition, four runs of 400 cycles each were conducted. A programmable timing unit (PTU X, LaVision) synchronized the excitation and detection systems. Recording commenced at

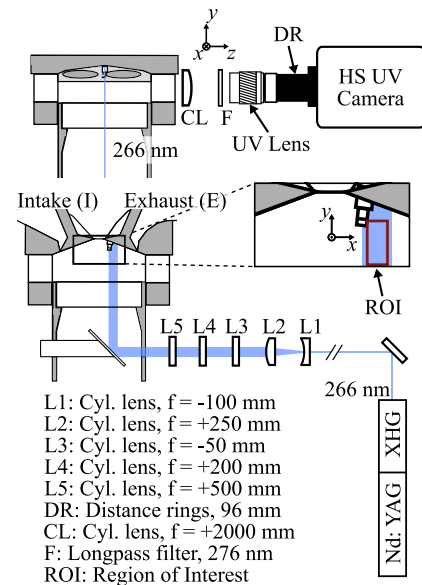


Fig. 1. Schematic of experimental setup and optical arrangement.

-0.8 °CA after ignition (°CA_{ai}) and -1.4 °CA_{ai} for OC α and A, capturing 45 and 31 images per cycle, respectively. To ensure repeatability, each set of 400 cycles is obtained through the following procedure: 300 fired warm-up cycles and 150 non-fired cycles preceded 500 measurement cycles, with the last 400 used for analysis.

It is important to note that our experimental method is limited to 2D, whereas the phenomenon of study is inherently 3D. For example, flame front curvature values taken from a 2D projection are different from the full 3D surface. This discrepancy is enhanced for H_2 flames [22]. However, a compromise between additional dimensions and resolution needs to be done in order to capture the small TDI cells.

2.2. Data processing

2.2.1. Image processing

The raw images were first denoised using wavelet-based denoising [16]. This denoising technique takes into consideration the camera characteristics and it is edge preserving, which is highly desirable in the detection of TDI cells. After that, the images were dewarped and scaled from pixel to real world coordinates using a 3rd order polynomial fit, obtained from a custom high-resolution calibration plate. Next, masking of the spark plug and piston was done. Laser energy correction was applied to each image using the laser profile derived from the average of the full combustion images for OC α , whereas for OC A, the profile was determined from the corrected image's respective crank angle average due to a consistent drift of the laser position. The images were then normalized to the maximum intensity of their respective cycle. Binarized flame images were obtained for each image using Otsu's method to find the threshold intensity [23]. Binarized flame structures smaller or equal to 6084 μ m² (composed of 25 pixels) were removed and holes within a binarized region were filled.

2.2.2. TDI marker

The presence of TDI cells was evaluated using a marker adapted from [24] that correlates the intensity gradient and curvature along the flame front's arc-length—leveraging the higher gradient at cell tips and lower gradient at creases. This study used the SO_2 -LIF intensity gradient (instead of the OH signal from the original work) and, although previous research has only demonstrated that SO_2 is a suitable tracer for the engine environment for CH_4 [15], the gradient at the H_2 flame front for the current setup (see Fig. 2a) clearly shows distinguishable

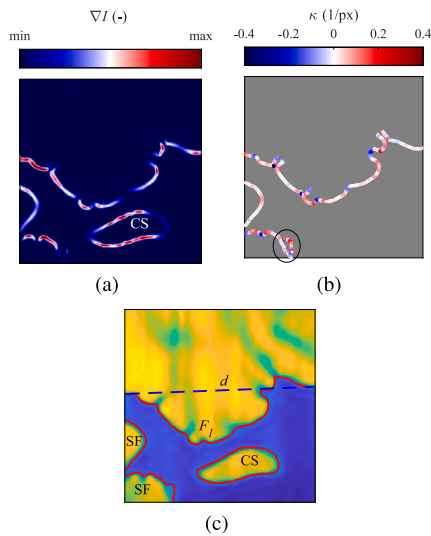


Fig. 2. Example image of the (a) intensity's gradient, (b) flame front's curvature and (c) energy-corrected image with F_l and d of the flame.

cell tips and creases. The intensity gradient and flame front curvature were computed using the Filtered Canny algorithm [25]. The initial flame front used to obtain the euclidean distance map was the flame front of the original binarized images. After that, a flame front mask consisting of all pixels with a distance less than or equal to 15 px of the initial front, was used to obtain the filtered gradient map. The final arc-length used for the computation of the marker is a result of non-maxima suppression of the masked gradient image, thinning the flame front to a unity pixel thickness curve. Curvature, κ , was calculated from the intensity gradient ∇I as $\kappa = -\nabla \cdot (\nabla I / |\nabla I|)$ analogous to the formula proposed in [26]. After that, the values corresponding to the front were extracted for the remaining computations. Note that closed structures were not considered for this analysis; for example, the closed structure below the main flame front in the intensity gradient image (labeled CS in Fig. 2a) was removed when obtaining the curvature values (Fig. 2b). Additionally, flame fronts shorter than 30 pixels were discarded to minimize non-realistic artifacts, whose contributions are assumed negligible.

The final TDI marker R is defined as the Pearson correlation coefficient between curvature and intensity gradient along the flame front obtained through the Filtered Canny algorithm. Higher R values indicate stronger development of TDI cells. Note that some small artifacts remain, such as the one highlighted with the ellipse in Fig. 2b. Nonetheless, their rarity and small size contribute negligibly to the final R value.

2.2.3. Flame wrinkling factor

While the previously introduced TDI Marker quantifies the visual presence of TDI cells, it does not capture flame front morphology. To independently assess flame front wrinkling, we define a wrinkling factor $\Omega = F_l/d$, where F_l is the measured flame front length within the ROI and d is the straight-line distance between its endpoints—analogue to the three-dimensional factors in [6] (see Fig. 2c). Closed flame fronts were rejected (e.g., CS in Fig. 2c), as were those with d less than 70% of the ROI's width (≈ 3 mm) (e.g., SF in Fig. 2c). Finally, if multiple disconnected fronts were left, an F_l -weighted average Ω was computed for each image. A value of $\Omega = 1$ indicates a perfectly straight flame front, while higher values reflect increased wrinkling.

3. Results and discussion

Images of example cycles for each OC are shown in Fig. 3 with their corresponding values of Ω and R , where NaN indicates that the

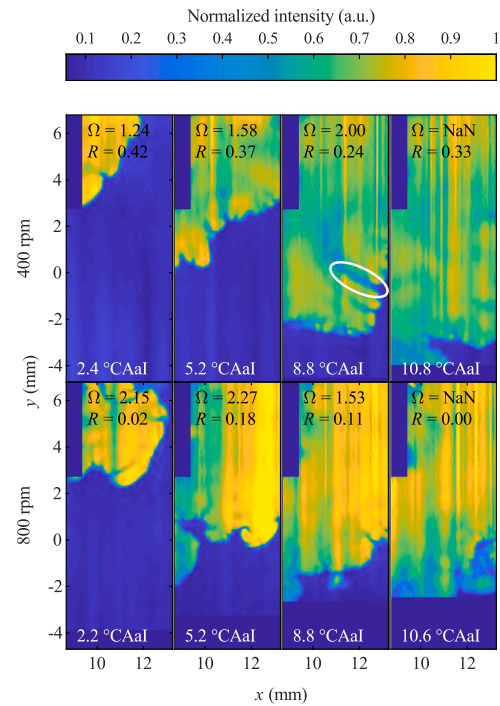


Fig. 3. Example of energy corrected images through a cycle for the 400rpm (top row) and 800rpm (bottom row) OCs.

value was not possible to compute due to no valid fronts remaining after the criteria set for the corresponding parameter. Even though energy correction was applied, the shot-to-shot laser fluctuations and beam steering effects, are still noticeable in the vertical stripe pattern of the signal. However, the images have enough signal-to-noise ratio for flame front analysis. TDI cells are distinctly detected for both conditions, specially for the timings of 5.2 °CAaI and 8.8 °CAaI. Larger and more striking cells are present for the 400rpm case, where even the so-called “finger-like” structures and accompanying sharp creases, characterized by the lower temperature and deeper regions, can be identified (highlighted region for 400rpm, 8.8 °CAaI). The levels of cell prominence are properly reflected in the TDI Marker value, testified by the values between the two OCs and visual identification of the stronger prominence for the 400rpm condition. Nevertheless, care needs to be taken when interpreting the values. At 2.4 °CAaI 400rpm, visual inspection shows that the cells are not very developed. The early flame kernel's smaller front and mainly positive curvature with the coincidental small crease with lower intensity led to a presumably inaccurate high R value. These conditions occur mainly in some early flame images, however it is not the norm. The equivalent image for 800rpm indicates a lower R value, correctly representing the lack of fully developed TDI cells. Notwithstanding, the shown early flames do have creasing and folded regions indicating a possible onset of TDI, similar to research by [6] where the onset of cellular structures is demonstrated to be enhanced by turbulence.

The flame wrinkling factor, Ω , also well represents its respective visible feature. Flames with fronts that deviate more from a straight line have higher values, confirmed by comparing the 5.2 °CAaI images. Nevertheless, the wrinkling factor is inflated for some early flames. The 800rpm early flame image shows an $\Omega = 2.15$ due to its smaller size. Here the flame front minimum distance was still larger than the defined criteria, even though the shape of the flame front within the ROI is clearly different from the further developed flames. This and the previously mentioned R early flame inaccuracies are statistically consistent across both OCs allowing us to compare their values statistically from cycle-to-cycle.

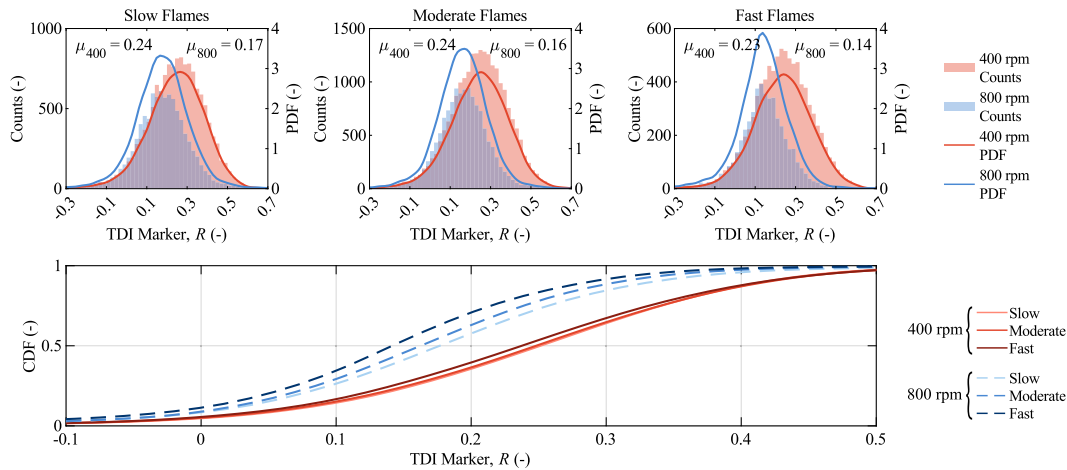


Fig. 4. Distribution of R values for the slow, moderate and fast cycles. Upper row: histogram and PDF with the mean values for the respective conditions' μ . Bottom row: CDF.

Independent evaluation of the TDI cells' prominence and flame front wrinkling is done first. After that, an analysis taking both features into account is presented. For these analyses, the cycles are separated into three classes: slow, moderate and fast flames. They are classified according to the mean flame growth $\bar{G} = \max(A_{\text{flame}})/t_{\text{max } A}$ of the cycle within the ROI, where $\max(A_{\text{flame}})$ is the maximum flame area obtained from the binarized flames and $t_{\text{max } A}$ is the time after ignition that the maximum area was reached. Within the same OC, cycles are classified based on \bar{G} : the lower quartile as slow flames, the second and third quartiles as moderate flames, and the last quartile as fast flames.

3.1. Prominence of TDI cells

The distribution of the R values for the different flame classes is shown in Fig. 4. These results pertain to all 1600 cycles per OC and all images where the computation of the TDI Marker was possible. A general difference of distributions is observed between the two OCs. Although the distributions between both conditions overlap, a clear shift to higher values exists for the 400rpm condition, showcasing more prominent TDI cells than the faster engine speed case. Looking at the CDF plot, for both conditions, the faster flames have lower R values. The difference is clearer for the 800rpm case, while for 400rpm, the difference between slow and moderate flames is much smaller than the one between moderate and fast ones.

The larger disparity between OCs stems from the significantly greater difference in turbulence intensity between the two conditions. A similar conclusion is drawn in [7] where higher-turbulence jet flames have an increased turbulent transport that overtakes molecular diffusion, leading to less regions of concentrated heat release typical of TDI. Across different OCs, the turbulence contrast is so pronounced that it affects cell development more noticeably. By contrast, variations within each OC are smaller because the turbulence differences between flame classes are less significant than those between OCs.

With cycle-to-cycle variations (CCV) and different OCs, factors such as temperature, pressure, and flame development time vary. Indeed, one can question if the observed cell development differences are mainly due to those parameters. To tackle this question, a dependency analysis on these parameters is done.

The unburned gas temperature difference between both OCs can be estimated via an isentropic assumption as explained in Section 2.1. For the timings of 0°C AaI, 8°C AaI and 16°C AaI, the estimated differences are 45 K, 34 K and 11 K respectively. Considering combustion, a conservative estimate places the maximum temperature difference at a given timing of less than 100 K. DNS studies carried out by [5], at 1 bar, show that a shift of unburned gas temperature from 500 K to 700 K leads to a

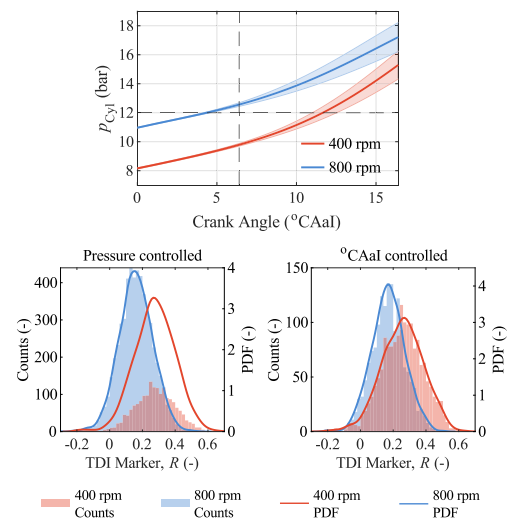


Fig. 5. Top: Pressure trace for both conditions with respect to crank angle after ignition. Solid lines: Mean. Shaded areas: standard deviation. Dashed lines: conditions from which the pressure and °CAaI controlled R values are taken. Bottom: R distributions for pressure and °CAaI controlled conditions.

difference of cell size of around 35%. The differences observed in Fig. 3 at 5.2°C AaI between the two OCs is of approximately 50% to 100%. Even considering the rough estimates, it is unlikely that the differences in cell development between the two OCs are mainly caused by the unburned gas temperature.

The pressure trace with respect to °CAaI is shown in the top of Fig. 5 and the R distribution regarding flames meeting specific conditions in the bottom. For the pressure controlled analysis, the R distribution of flames where the p_{Cyl} was within 12 ± 0.25 bar are shown. A timing of 6.4°C AaI was taken for the timing controlled case. Both analyses show the same results: R is distributed distinctly between the different engine speeds, showcasing independence of the distributions relative to these two parameters. Therefore, pressure and timing also cannot be assumed as the main contributors for the discrepancy of TDI cell development between OCs. Based upon the given evidence, turbulence is taken to be the most crucial influencing factor on cell development for the tested conditions. We emphasize that this argument does not suggest unburned gas temperature, pressure, and timing have no influence on TDI cells in an internal combustion engine, but rather that their effect is weaker compared to turbulence.

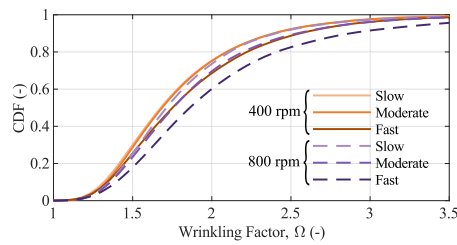


Fig. 6. Distribution of Ω values for the slowest, moderate and fastest cycles of both OCs.

3.2. Flame front wrinkling

In contrast to the distributions of R , Ω values across the two evaluated engine speeds are less distinguishable (see Fig. 6). Nevertheless, results still indicate differences between OCs and flame classes. As for the differences between OCs, the 400 rpm case has lower wrinkling (a shift of the curves to lower Ω values), specially noticeable when comparing the same flame classes. The difference between the two engine speeds increases from slow to fast flames: the difference in distribution is almost minimal between slow flames, but a larger discrepancy is seen for the fast flames.

As for the differences within OCs, faster flames have higher wrinkling levels. The shift is noticeable for all flame classes in both engine speeds except for 400 rpm between slow and moderate flames. Similarly to R , the difference in turbulence between these two classes is not high enough to stimulate changes in the wrinkling level. For the 800 rpm condition, however, the turbulence difference is high and strong enough to shift the Ω distributions between all flame classes.

The flame wrinkling differences within a constant engine speed contrast with those observed across engine speeds—opposite to the behavior of the TDI marker. Specifically, a substantial increase in turbulence across engine speeds yields smaller variations in the Ω distribution, whereas a modest increase between flame classes produces larger differences. This occurs because our analysis, confined to a small ROI, captures mainly small-scale turbulence-driven perturbations while filtering out larger-scale turbulence and bulk-flow effects. Consequently, the Ω value does not entirely reflect the full flame front's morphology. Additionally, these results underscore that turbulence is the main driver for the faster flames. Since the bulk flow structures are effectively filtered by our small ROI, the observed increase in wrinkling for faster flames within the same OC comes from turbulence or TDI cells. Considering the previous results, where TDI cells are more pronounced for slower flames, by process of elimination, turbulence remains as the main driver for the faster flames.

To capture the effects of larger flow and turbulence structures on flame propagation, a larger ROI would be needed; however, this would reduce the optical resolution, hindering the detection of smaller TDI induced structures. In this regard, three-dimensional analysis obtained from computational fluid dynamics (CFD) or experimental methods such as high-speed scanning particle image velocimetry (PIV) [27], would improve the understanding of turbulence's effects. Nevertheless, the employed setup detects increased wrinkling for cycles with higher expected turbulence.

3.3. Interaction between TDI cells and flame wrinkling

Although the previous analyses treated each feature separately, it is important to note that TDI cells and flame wrinkling are intrinsically linked. Such interplay is shown by [28], demonstrating a synergistic relationship between turbulence and TDI induced “tongue-like shapes”, akin to the cellular structures seen for the engine. In light of this, we further examine their correlation in this section.

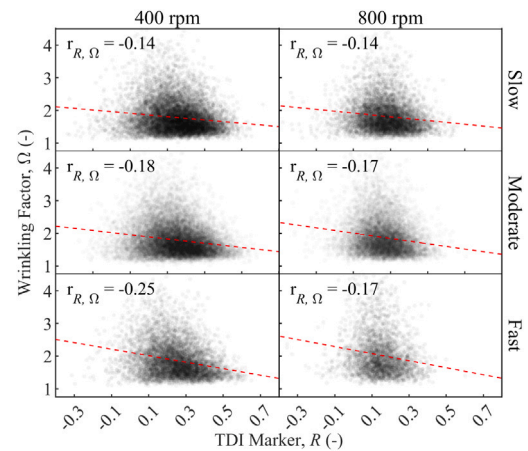


Fig. 7. Correlation between Wrinkling Factor Ω and TDI Marker R . Pearson correlation coefficient $r_{R,\Omega}$ is given for each condition. The red dashed line indicates the linear regression for visualization purposes. All correlations are significant at the 99% confidence level.

Fig. 7 presents the correlation between R and Ω across different OCs and flame classes for all flames with valid R and Ω computed values. Overall, the correlations are negative, indicating that TDI cells are more prevalent in less wrinkled flames. The stronger negative correlation in the 400 rpm fast flame class reflects the more developed TDI cells. Higher turbulence in faster flames affects the front, making its effects more noticeable in cell development. Thus, the relationship between flame front wrinkling and TDI cell development is inverse. When turbulence is weaker, the flame front remains less disturbed, allowing cell development to be more pronounced. Fig. 8 illustrates these extremes: a less disturbed flame front accompanies the clear presence of cells, whereas a highly distorted flame front shows less signs of TDI cells. These results align with experiments conducted in a constant volume vessel for spherical flame propagation, which demonstrated that turbulence causes greater flame surface wrinkling than non-turbulent flames that exhibit only intrinsic instabilities [29]. At higher, more realistic engine speeds, the morphological aspect of TDI cell formation becomes less pronounced, which could be taken into account in H_2 flame modeling. Additionally, TDI-induced flame speed enhancement still plays a major role in flame dynamics. Other consequences, such as the increase in turbulent flame speed has been shown to be caused by the enhanced reactivity of the flame front rather than the increase in flame area [8]. Moreover, higher local heat release rate in turbulence-induced positive flame curvature regions have been demonstrated numerically [30]. Yet, experiments in turbulent jet flames have shown that this increase in heat release becomes less pronounced, almost negligible, with intensified turbulence—reflected in a higher Karlovitz number (Ka) [7]. Therefore, the question remains as to how the increase in heat release behaves in engines.

4. Conclusions

Planar SO_2 -LIF, with high spatial and temporal resolution, was used to capture H_2 flames in an optically accessible ICE operating at 400 rpm and 800 rpm with $\lambda = 2.5$. The achieved optical resolution was sufficient to resolve TDI cells and their detection in the dynamic ICE environment was demonstrated. This work focused on assessing the influence of engine speed on both TDI cell development and flame wrinkling by employing distinct markers for each feature, with visual inspection confirming their suitability for statistical analysis. Results indicate that TDI cell development is markedly more pronounced at 400 rpm and in slower flames within the same OC. A dependency analysis on unburned gas temperature, pressure, and timing shows that these factors do

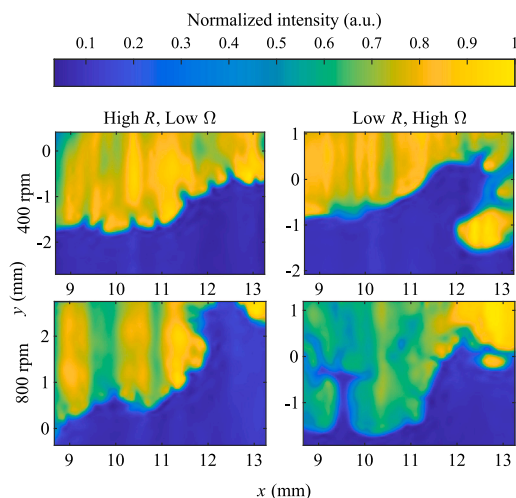


Fig. 8. Detailed view of example images of the negative correlation between TDI cell development and flame front wrinkling. Top row: 400 rpm. Bottom row: 800 rpm. Left column: high cell development. Right column: high flame wrinkling.

not account for the observed differences, implicating turbulence as the primary driver for mitigating TDI cell development. At 800 rpm and in faster flames, increased turbulence disrupts TDI cell formation while enhancing flame wrinkling; at 400 rpm, the differences between flame classes are less pronounced. Overall, the data reveal an inverse relationship between TDI cell development and flame front wrinkling.

Morphologically, flame wrinkling does not significantly increase with TDI cell formation; rather, cell development thrives in the absence of significant wrinkling. This suggests that at higher engine speeds, TDI cell formation is significantly mitigated. Nevertheless, the enhancement of flame speed due to TDIs must be considered. Additionally, increased local heat release in positively curved flame regions, the associated higher NO_x formation, and impacts on wall heat transfer and flame quenching remain open topics in H_2 engine research.

To fully understand flame-wall interactions in H_2 -fueled ICES, high-resolution wall temperature measurements are required. In addition, capturing global flame propagation relative to the instantaneous engine flow field would greatly enhance our understanding of flame wrinkling and overall propagation dynamics. Consequently, further research into TDI in ICES is essential for accurately modeling and advancing H_2 -fueled engine development.

Novelty and significance statement

This study presents high-resolution imaging of H_2 flames in an optically accessible internal combustion engine (ICE), clearly capturing thermodiffusive instability (TDI) cells—the first of its kind to the authors' knowledge. It provides a distinct evaluation of the prominence and formation of TDI cells, as well as flame front wrinkling, offering new insights into their interplay. The effects of engine speed on TDI behavior are analyzed, revealing a negative correlation between TDI cell development and flame wrinkling. These findings contribute to a deeper understanding of cell formation in an ICE under varying speeds, suggesting that at higher, more realistic engine speeds, TDI cells might play a less dominant role in flame dynamics.

CRediT authorship contribution statement

Pedro Ye: Conducted experiments, Processed and analyzed data, Writing – original draft, Organized the submission. **Jannick Erhard:**

Conducted experiments, Processed data, Assisted the analysis, Reviewed and edited the manuscript. **Cooper Welch:** Conducted experiments, Assisted the analysis, Reviewed and edited the manuscript. **Hao Shi:** Reviewed and edited the manuscript. **Andreas Dreizler:** Reviewed and edited the manuscript. **Benjamin Böhm:** Acquired funding, Assisted the analysis, Reviewed and edited the manuscript, Supervised.

Declaration of competing interest

The authors declare that they have no known competing financial interests or personal relationships that could have appeared to influence the work reported in this paper.

Acknowledgments

Support by Deutsche Forschungsgemeinschaft, Germany through FOR 2687 “Cyclic variations in highly optimized hydrogen-fueled spark-ignition engines: experiment and simulation of a multi-scale causal chain”—project number 423224402—is kindly acknowledged.

References

- [1] S. Verhelst, T. Wallner, Hydrogen-fueled internal combustion engines, *Prog. Energy Combust. Sci.* 35 (6) (2009) 490–527.
- [2] A. Onorati, R. Payri, B.M. Vaglieco, A.K. Agarwal, C. Bae, G. Bruneaux, M. Canakci, M. Gavaises, M. Günthner, C. Hasse, S. Kokjohn, S.-C. Kong, Y. Moriyoshi, R. Novella, A. Pesyridis, R. Reitz, T. Ryan, R. Wagner, H. Zhao, The role of hydrogen for future internal combustion engines, *Int. J. Engine Res.* 23 (4) (2022) 529–540.
- [3] H. Pitsch, The transition to sustainable combustion: Hydrogen- and carbon-based future fuels and methods for dealing with their challenges, *Proc. Combust. Inst.* 40 (1–4) (2024) 105638.
- [4] C. Bauwens, J.M. Bergthorson, S.B. Dorofeev, Experimental investigation of spherical-flame acceleration in lean hydrogen-air mixtures, *Int. J. Hydrog. Energy* 42 (11) (2017) 7691–7697.
- [5] L. Berger, A. Attili, H. Pitsch, Intrinsic instabilities in premixed hydrogen flames: parametric variation of pressure, equivalence ratio, and temperature. Part 2 – non-linear regime and flame speed enhancement, *Combust. Flame* 240 (2022) 111936.
- [6] H. Chu, L. Berger, T. Grenga, Z. Wu, H. Pitsch, Effects of differential diffusion on hydrogen flame kernel development under engine conditions, *Proc. Combust. Inst.* 39 (2) (2023) 2129–2138.
- [7] S. Shi, R. Schultheis, R.S. Barlow, D. Geyer, A. Dreizler, T. Li, Internal flame structures of thermo-diffusive lean premixed H_2 /air flames with increasing turbulence, *Proc. Combust. Inst.* 40 (1–4) (2024) 105225.
- [8] G. Troiani, P.E. Lapenna, F. D'Alessio, F. Creta, Scaling transition of turbulent flame speed for thermodynamically unstable flames, *Phys. Fluids* 36 (11) (2024).
- [9] V. Salazar, S. Kaiser, Influence of the flow field on flame propagation in a hydrogen-fueled internal combustion engine, *SAE Int. J. Engines* 4 (2) (2011) 2376–2394.
- [10] C. Ramalho Leite, P. Brequigny, J. Borée, F. Foucher, Early flame development characterization of ultra-lean hydrogen-air flames in an optical spark-ignition engine, *Proc. Combust. Inst.* 40 (1–4) (2024) 105260.
- [11] C. Welch, J. Erhard, H. Shi, A. Dreizler, B. Böhm, An experimental investigation of lean hydrogen flame instabilities in spark-ignition engines, *Proc. Combust. Inst.* 40 (1–4) (2024) 105391.
- [12] F. Zentgraf, E. Baum, B. Böhm, A. Dreizler, B. Peterson, On the turbulent flow in piston engines: Coupling of statistical theory quantities and instantaneous turbulence, *Phys. Fluids* 28 (4) (2016).
- [13] N. Fogla, F. Creta, M. Matalon, The turbulent flame speed for low-to-moderate turbulence intensities: Hydrodynamic theory vs. experiments, *Combust. Flame* 175 (2017) 155–169.
- [14] W. Kirchweger, R. Haslacher, M. Hallmannssegger, U. Gerke, Applications of the LIF method for the diagnostics of the combustion process of gas-IC-engines, *Exp. Fluids* 43 (2–3) (2007) 329–340.
- [15] R. Honza, C.-P. Ding, A. Dreizler, B. Böhm, Flame imaging using planar laser induced fluorescence of sulfur dioxide, *Appl. Phys. B* 123 (9) (2017).
- [16] J. Weinkauff, P. Trunk, J.H. Frank, M.J. Dunn, A. Dreizler, B. Böhm, Investigation of flame propagation in a partially premixed jet by high-speed-Stereo-PIV and acetone-PLIF, *Proc. Combust. Inst.* 35 (3) (2015) 3773–3781.
- [17] E. Baum, B. Peterson, B. Böhm, A. Dreizler, On the validation of LES applied to internal combustion engine flows: Part 1: Comprehensive experimental database, *Flow Turbul. Combust.* 92 (1–2) (2014) 269–297.
- [18] C. Welch, L. Illmann, M. Schmidt, B. Böhm, Experimental characterization of the turbulent intake jet in an engine flow bench, *Exp. Fluids* 64 (5) (2023).

- [19] J.K. Bechtold, M. Matalon, The dependence of the Markstein length on stoichiometry, *Combust. Flame* 127 (1–2) (2001) 1906–1913.
- [20] D.G. Goodwin, H.K. Moffat, I. Schoegl, R.L. Speth, B.W. Weber, *Cantera: An object-oriented software toolkit for chemical kinetics, thermodynamics, and transport processes*, 2023.
- [21] S. Bürkle, L. Biondo, C.-P. Ding, R. Honza, V. Ebert, B. Böhm, S. Wagner, In-cylinder temperature measurements in a motored IC engine using TDLAS, *Flow, Turbul. Combust.* 101 (1) (2018) 139–159.
- [22] Y. Zheng, P. Ahmed, S. Hochgreb, 3D flame surface curvature analysis from reconstructed scanning across spherical expanding flames, *Proc. Combust. Inst.* 40 (1–4) (2024) 105688.
- [23] N. Otsu, A threshold selection method from gray-level histograms, *IEEE Trans. Syst. Man Cybern.* 9 (1) (1979) 62–66.
- [24] O. Chaib, S. Hochgreb, I. Boxx, An experimental marker of thermo-diffusive instability in hydrogen-enriched flames, *Proc. Combust. Inst.* 40 (1–4) (2024) 105763.
- [25] O. Chaib, Y. Zheng, S. Hochgreb, I. Boxx, Hybrid algorithm for the detection of turbulent flame fronts, *Exp. Fluids* 64 (5) (2023) 104.
- [26] X. Wen, T. Zirwes, A. Scholtissek, H. Böttler, F. Zhang, H. Bockhorn, C. Hasse, Flame structure analysis and composition space modeling of thermodynamically unstable premixed hydrogen flames — Part I: Atmospheric pressure, *Combust. Flame* 238 (2022) 111815.
- [27] J. Bode, J. Schorr, C. Krüger, A. Dreizler, B. Böhm, Influence of the in-cylinder flow on cycle-to-cycle variations in lean combustion DISI engines measured by high-speed scanning-PIV, *Proc. Combust. Inst.* 37 (4) (2019) 4929–4936.
- [28] L. Berger, A. Attili, H. Pitsch, Synergistic interactions of thermodynamically unstable and turbulence in lean hydrogen flames, *Combust. Flame* 244 (2022) 112254.
- [29] Y. Xie, J. Yang, P. Ahmed, B.J.A. Thorne, X. Gu, Three-dimensional dynamics of unstable lean premixed hydrogen-air flames: Intrinsic instabilities and morphological characteristics, *Combust. Flame* 271 (2025) 113800.
- [30] T.L. Howarth, E.F. Hunt, A.J. Aspden, Thermodynamically-unstable lean premixed hydrogen flames: Phenomenology, empirical modelling, and thermal leading points, *Combust. Flame* 253 (2023) 112811.